Arch. Metall. Mater. **65** (2020), 3, 1227-1238

DOI: 10.24425/amm.2020.133654

N. SOBCZAK[1,2*], M. BACIOR[3], P. TURALSKA[4], G. BRUZDA[4], M. HOMA[4], J.J. SOBCZAK[5]

THE INFLUENCE OF ALLOYING ADDITIONS ON HIGH TEMPERATURE INTERACTION BETWEEN MOLTEN COMPACTED GRAPHITE IRON AND ALUMINA

High temperature behavior of three compacted graphite iron (CGI) alloys on polycrystalline alumina substrates (99.7%, porosity <3%) were examined by the sessile drop method combined with classical contact heating procedure in flowing Ar. High-speed high-resolution CCD camera was used for continuous recording of the CGI/Al_2O_3 couples during melting alloy, heating to and holding the couples at the test temperature of 1450°C for 15 min and their subsequent cooling. The comparative studies were made with conventional CGI (in wt.%: 3.70 C, 2.30 Si, 0.44 Mn, 0.054 P, 0.017 Mg, 0.015 S) and two alloys additionally containing the same amounts of 0.25 Mo, 0.1 V, 0.045 Sn and 0.032 Sb with different concentrations of Mg + Cu additions, i.e. 0.01Mg + 0.33Cu and 0.02Mg + 0.83Cu. All three CGI alloys demonstrated non-wetting behavior on the Al_2O_3 substrates while the contact angle values slightly decreased with increase of the Mg + Cu content in the alloy, i.e. 131° (unalloyed CGI), 130° (0.01Mg + 0.33Cu) and 125° (0.02Mg + 0.83Cu). Structural characterization of solidified couples by light microscopy and scanning electron microscopy coupled with energy dispersive X-ray spectroscopy revealed: 1) heterogeneous nucleation of discontinuous graphite layer at the drop-side interfaces and on the surface of the drops; 2) reactively formed Mg-rich oxide layer at the substrate-side interface; 3) the formation of satellite droplets on the surface of the drops during their solidification; 4) degeneration of initially compacted graphite to lamellar graphite after remelting and subsequent solidification of the drops, particularly in their surface layer.

Keywords: compacted graphite iron, Al_2O_3, sessile drop method, wettability, interface

1. Introduction

Cast iron is one of the oldest man-made alloys that has played revolutionary role in the development of human civilization [1]. It belongs to a family of casting alloys that is still most used for the production of industrial components due to its low cost combined with unique characteristics such as good castability and machinability, the wide range of mechanical properties, excellent friction and wear characteristics [1-4]. Traditionally, cast iron is Fe-based alloy that has 2-4 wt% carbon and 1-3 wt% silicon. It has heterogeneous structure, in which the carbon may exist in the form of different precipitates, whose morphology and chemistry depend on the alloy chemical composition as well as on molten metal and post-processing treatments [1-4]. Cast irons, in which carbon is present in iron carbide (cementite) are called "white" cast iron while those with graphite precipitates are named "grey" cast iron. Depending on the shape of graphite precipitates, three types of grey cast iron are distinguished: 1) lamella graphite iron with flake-like graphite (LGI) of elongated shape, 2) spheroidal graphite cast iron (SGI), also known as ductile iron, with nearly-spherical graphite precipitates and 3) compacted (vermicular) cast iron (CGI), in which graphite is present in a worm-like, stubby form with rounded edges.

In terms of its microstructure and combination of mechanical and physical properties, CGI falls between cast iron with flake-like graphite and cast iron with spheroidal graphite. Compared to conventional grey cast iron, CGI has almost double tensile strength and fatigue strength, 38% higher elastic modulus and 8% smaller thermal conductivity [5]. This beneficial combination of materials properties justifies a wide application of CGI in manufacturing of components for trucks, tractors, passenger cars and marine diesel engines [2-4] and more recently, for the production of cylinder blocks for diesel engines or railway brake discs [6-10].

Many studies contributed to understanding factors affecting the structure-properties relationships of cast irons and

[1] INSTITUTE OF METALLURGY AND MATERIALS SCIENCE, POLISH ACADEMY OF SCIENCES, 25 REYMONTA STR., 30-059 KRAKOW, POLAND
[2] LUKASIEWICZ RESEARCH NETWORK – INSTITUTE OF PRECISION MECHANICS, 3 DUCHNICKA STR., 01-796 WARSAW, POLAND
[3] UNIVERSITY OF AGRICULTURE IN KRAKOW, DEPARTMENT OF PHYSICS, A. MICKIEWICZA AV. 21, 31-120 KRAKOW, POLAND
[4] LUKASIEWICZ RESEARCH NETWORK – KRAKOW INSTITUTE OF TECHNOLOGY, 73 ZAKOPIAŃSKA STR., 30-418 KRAKOW, POLAND
[5] AGH UNIVERSITY OF SCIENCE AND TECHNOLOGY, FACULTY OF FOUNDRY ENGINEERING, 23 REYMONTA STR., 30-059 KRAKOW, POLAND

* Corresponding author: n.sobczak@imim.pl

particularly, the nucleation and grows of graphite phase from Fe-C melts (e.g. [11-20]). It was evidenced experimentally that different additions can modify both the matrix microstructure and graphite morphology and thus influence on the performance of cast iron. The silicon and some rare earth elements can transform the graphite morphology from flake-like to vermicular-like or spherical-like. To improve the properties of CGI, alloying additions such as copper, molybdenum, vanadium, antimony, and tin are used. Studies on the impact of single alloying additions to CGI, e.g. copper in the range of 0.6-0.8%, tin in the range of 0.27-0.28%, manganese in the range of 0.2%-0.9%, demonstrated an increase in the amount of perlite [12]. Small amounts of alloying additions, such as Cu, Mo, V, Sn and Sb, increase the thermal fatigue resistance of this kind of cast iron [13]. Copper dissolved in austenite inhibits the diffusion of carbon and lowers the temperature of eutectoidal transition [4], which causes the formation of fine-grained perlite. It also increases the amount of nodular graphite from the vermicular graphite [14]. Higher amount of perlit in the metal matrix increases the value of the tensile strength and decreases the CGI plasticity [15]. Copper is known also to increase the corrosion resistance and to improve the wear resistance of cast iron and graphitized steel. In eutectic crystallization of cast iron, copper contributes to the removal of ledeburitic chilling, disintegration of eutectic structure and it is a graphitizing element [16-20]. It increases the pearlitization degree of the structure and reinforces the stability and dispersity of eutectoid cementite [18] thus affecting the mechanical properties of cast iron. By hardening ferrite and pearlite, copper increases the strength and hardness of cast iron. The microhardness of copper-alloyed pearlite can reach 600-700 HV or higher [17]. However, too high content of copper (over 5%) does not improve the properties of cast iron [20] but makes it more expensive.

For structure-properties relationships of cast iron, graphite morphology is of crucial importance and many studies were dedicated to understanding the mechanisms and factors influencing solidification, especially graphite nucleation and grows [20-28] as well as volume change during solidification [29,30]. It is widely accepted that the formation of graphite particles in molten cast iron takes place through heterogeneous nucleation, in which even small additions in an alloy may play an important role, particularly those that can form non-metallic inclusions (e.g. sulfides, oxides, carbides), acting as seeds for nucleation of graphite phase. Scientific concepts based on the impurity level in the Fe-C melt claim that the final morphology of graphite precipitates is the consequence of the interaction between the reactive compacting elements (e.g. Mg, Ce) and the surface-active anti-compacting elements (e.g. O, S). Therefore, the improvement of physical and mechanical properties of cast iron components is possible through controlled transition LG-to-CG-to-SG by decreasing amounts of anti-compacting impurities and increasing amounts of compacting impurities [20-28].

Further improvement of the cast iron performance, particularly its wear resistance, is possible through introduction of ceramic reinforcements to produce metal matrix composites (MMCs) [31], in which cast iron is a metal matrix while reinforcing ceramics can be in the form of particles uniformly incorporated within a metal matrix [31,32], porous preforms infiltrated with metal matrix [31] or bulk inserts used for local reinforcement of metal castings [33]. All liquid-assisted pressureless processes of MMCs require good wetting of a ceramic by a molten metal matrix [34], i.e. the contact angle value of $\theta \ll 90°$ as a prerequisite condition to manufacture high-quality final products. Therefore, information on the wetting phenomena taking place in different cast iron/ceramic systems at elevated temperatures constitutes both scientific and practical importance.

Due to low cost of oxide particles, compared to those of various metal carbides and nitrides used as reinforcing phases (e.g. titanium, tungsten, molybdenum carbides or nitrides), metal oxides might be attractive candidates for reinforcing ferrous alloys [31-33]. Among different oxides, Al_2O_3 is widely used in nonferrous metallurgy practice to produce MMCs because of its reinforcing and anti-friction properties coupled with a low density. However, literature data on high-temperature interaction between molten cast iron and Al_2O_3 or Al_2O_3-rich refractories are very scarce [35-37]. Such information could be useful not only for synthesis of cast iron based MMCs but also for the production of high quality cast iron components free of such common casting defects as oxide inclusions because Al_2O_3-based refractories are widely used in metal casting practice for molds, crucibles, filters and other foundry appliances. This study is the continuation of the research reported in [38,39] and dedicated to understanding the issues altering physico-chemical compatibility between CGI matrix and oxides as reinforcing phases. It concerns comparative investigation of the effect of small additions to CGI on its high-temperature interaction with aluminum oxide, particularly wetting, reactivity, interface structure and chemistry as well as bonding between these two dissimilar materials.

2. Experimental

Two hypereutectic CGI alloys were used in this study (Table 1). In the as-cast condition, they contained comparable amounts of Mo, V, Sn and Sb additions but different Mg + Cu contents, i.e. 0.01Mg + 0.33Cu (CGI-1) and 0.02Mg + 0.83Cu (CGI-2) with the same saturation coefficient $Sc \rangle 1$. As-cast alloys

TABLE 1

The chemical composition of CGI samples in as-cast state (wt.%)

CGI	C	Si	Mn	P	S	Mg	Mo	Cu	V	Sn	Sb	Remarks
CGI-0	3.70	2.30	0.44	0.054	0.015	0.017	—	—	—	—	—	[24]
CGI-1	3.60	2.35	0.38	0.045	0.015	0.010	0.25	0.33	0.09	0.045	0.031	This study
CGI-2	3.85	2.07	0.38	0.050	0.020	0.020	0.25	0.83	0.12	0.05	0.032	This study

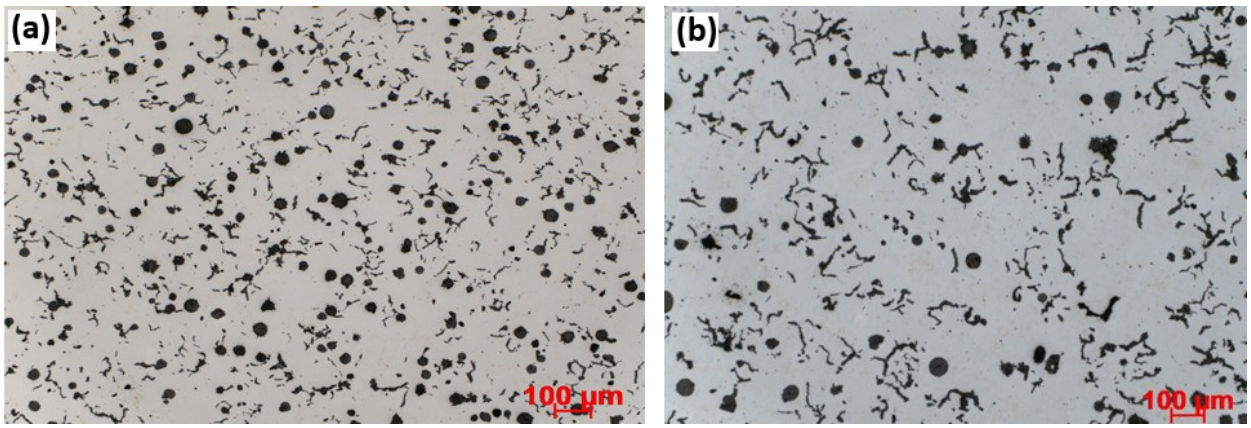

Fig. 1. LM micrographs showing the microstructure of examined CGI samples in as-cast state, metallographic cross sections: (a) CGI-1; (b) CGI-2

had pearlitic structure with estimated fraction of perlite above 98% and both CGI-1 (Fig. 1a) and CGI-2 (Fig. 1b) showed uniform distribution of graphite precipitates those amount was higher in case of high Mg + Cu content. Most graphite precipitates had vermicular morphology (60% in CGI-1 and 80% in CGI-2), the rest of them were spheroidal with both irregular (30% and 15%, respectively) and regular shape (10% and 5%, respectively). The average length of vermicular graphite was about few dozen micrometers in each alloy. The alloy samples were cut from the large ingot to get the samples with cubic shape of 5×5×5 mm size. Melting and casting trials of selected alloys were performed according with procedure described elsewhere [40].

A sessile drop method was adopted in this study for real-time observation of high temperature behavior of CGI samples during their heating, melting, wetting, cooling and subsequent solidification on alumina substrates. The substrates of a cylindrical shape (18 mm in diameter and 5 mm in height with open porosity below 3 vol.%) were produced by Ceramit (Poland) from commercial polycrystalline alumina powder of 99.7% purity. The testing surface of the substrates was polished to a roughness of R_a = 150 ±20 nm.

The sessile drop tests were performed in the experimental complex for high-temperature studies of liquid metals and alloys described in detail in [41,42]. In this study, "2in1" procedure was applied since it allows to test two couples in one experiment under the same testing conditions. For this purpose, cylindrical substrates were cut into two identical parts, which directly before placing in a vacuum chamber were cleaned in isopropanol and heated for 30 minutes at 1000°C. Next, the samples of two selected CGI alloys, mechanically and ultrasonically cleaned in isopropanol just before their loading into vacuum chamber, were placed on previously cleaned and heat-treated Al_2O_3 substrates and the alloy/substrate assembles were located on tantalum experimental table inside tantalum resistant heater of UHV chamber.

When gases were evacuated up to a pressure of $p = 6\times10^{-7}$ mbar, the couples of materials (CGI samples on Al_2O_3 substrates) were contact heated with a rate of 15°C/min up to 500°C, then flowing inert gas (Ar, 99.9992%) was introduced into a UHV chamber up to a pressure of p = 900 mbar. Next, the couples were heated up with the same rate to a test temperature of 1450°C and after 15 min isothermal heating, they were cooled down to room temperature with a rate of 20°C/min.

High-temperature interaction between the CGI samples and Al_2O_3 substrates was recorded using high-speed high-resolution CCD camera MC1310 with a rate of 10 fps (frames per second) during melting of metal sample and during isothermal heating, while during cooling, the recording was carried out at a rate of 1 fps. Collected images (Fig. 2a) were used to estimate the values of the contact angle by the ASTRA2 software (CNR-IENI, Italy [43,44]) and to make a real-time movie of the high-temperature test (Movie 1. Click here). The software enables to determinate the contact angle on the left (θ_l) and on the right (θ_r) sides of a drop by an automatic image analysis (systematic uncertainty of the contact angle <±2°).

The detailed structural investigation was performed on the solidified sessile drop couples using Keyence VHX-700F light microscope (LM) under the magnification up to 500× and Hitachi TM3000 scanning electron microscope (SEM) equipped with Quantax 70 Energy Dispersive X-ray Spectrophotometer (EDS) of Bruker Nano GmbH. For high resolution SEM observations accompanied with EDS analysis, FEI Scios™ DualBeam™ microscope equipped with EDS analyzer (Oxford Instruments Aztec) was used.

The results of this study were compared with those of our experimental data already reported for conventional CGI free of selected additions and obtained under the same testing conditions [38] (Sample CGI-0 in Table 1).

3. Results and discussion

The real time observation of melting of the alloys, its interaction with the alumina substrate and solidification process of CGI samples on the alumina substrates can be seen on the movie of the sessile drop test (Movie 1). Figure 2 illustrates the couples at the most important stages of the test, starting from room temperature (Fig. 2a). The melting process of initially solid CGI samples began at a temperature of about 1194°C while both samples got a shape typical for the drops at T = 1199°C, corresponding to the beginning of the wettability kinetics curve in

Figs. 3a,b. During further heating up to 1450°C and isothermal holding at that temperature, the drops changed its shape with corresponding increase in the drop/substrate contact area (Fig. 2c). Fig. 2d shows the last recorded image taken at the end of the wettability test at 1141°C (also shown in Figs. 3a,b).

As can be seen from the test movie (Movie 1) and Fig. 2d, during the cooling down of the couples, the formation of the small secondary satellite droplets (called "daughter" droplets) has started on the surface of the "mother" drops at a temperature of about 1141°C. The same observations were noted in our previous studies of the CGI-0/Al_2O_3 [38] and CGI-0/Al_2O_3-ZrO_2-SiO_2 [39] couples performed under the same testing conditions. We suggested that this phenomenon is associated with the outflow of melted, not yet solidified alloy from the interior of the main drop to its outside. It should be highlighted that in this study, the daughter droplets were formed mainly on the surfaces where the mother drops were neighboring to each other, i.e. in the space corresponding to the central part of the tantalum heater. This finding is experimental evidence of the role of non-uniform solidification of the drops accompanied with the phenomenon of volume expansion during solidification known for many cast irons (e.g. [29,30]). We may conclude that during cooling, testing conditions with flowing Ar contribute to non-uniform temperature around the drops resulting in slower cooling in the central part of the experimental table, where the mother drops were neighboring to each other. Therefore, the solidification of both drops starts outside of this space by forming a thin layer of solidified metal on the surface of both drops. During further cooling, the solidified layer covers whole drop surfaces. However, due to temperature gradient inside the heater space during cooling, the solidified layer has non-uniform thickness, i.e. the further is from the central part the thicker is this layer. Therefore, when an inner (still molten) residual metal solidifies, it protrudes through cracks (easily formed in the thinnest solid layer on the neighboring surfaces of two drops) due to expansion phenomenon taking place in CGI during liquid-to-solid transformation. These observations are in accordance with literature data [29,30] showing that the volume expansion of cast iron takes place mainly in the eutectic region having the lowest melting point, as compared to other constituents of cast irons. Therefore, the volume expansion continues until the end of solidification and it increases with an increase of the carbon content and the amount of magnesium residual.

The variations in contact angle (θ) with time and temperature for the CGI-1 and CGI-2 drops on the alumina surfaces during the sessile drop test are shown in Fig. 3a and Fig. 3b, respectively. The θ values corresponding to the most important stages of the test are collected in Table 2. The contact angles were measured from the recorded images of the couples starting from T = 1199°C when the metal samples were melted and got drop-like shape. At that temperature, both alloys did not wet the alumina substrate forming high left (θ_l^*) and right (θ_r^*) contact angles of 146° and 143° for CGI-1 and 150° and 144° for CGI-2, respectively. Further heating of the CGI/Al_2O_3 couples to the test temperature caused a decrease in the contact angle values. When the wettability test started at T = 1450°C (t = 0), the values of the contact angles of CGI-1 were θ_l = 131° and θ_r = 128°. During 15 minutes at the test temperature as well as during final cooling, this alloy did not show noticeable changes in contact angle values (Fig. 3a). On the contrary, the CGI-2 alloy having two times higher amount of Mg + Cu did not get stabilization and its wetting of alumina substrate was continuously improving with time even during cooling (Fig. 3b). For t = 0 at T = 1450°C, the CGI-2 drop had symmetrical shape evidenced by the same values of $\theta_l^0 = \theta_r^0$ = 128° that decreased after 15 minutes to θ_l^{15} = 126° and θ_r^{15} = 124° and next to the final values of θ_l^f = 122° and θ_r = 120°, recorded at 1145°C. Such behavior of metal/ceramic couples is usually related with either a strong evaporation from the melt [45,46] or the formation of interfacial reaction product that is better wettable than original substrate [34]. In case of examined couples, both mechanisms are possible as it is discussed below.

Visual observation of solidified alloys (Fig. 4, Fig. 5a) showed their bright surface typical for the drops free of continuous oxide film. However, both drops were partially covered with black spots corresponding to the graphite layer nucleated at the

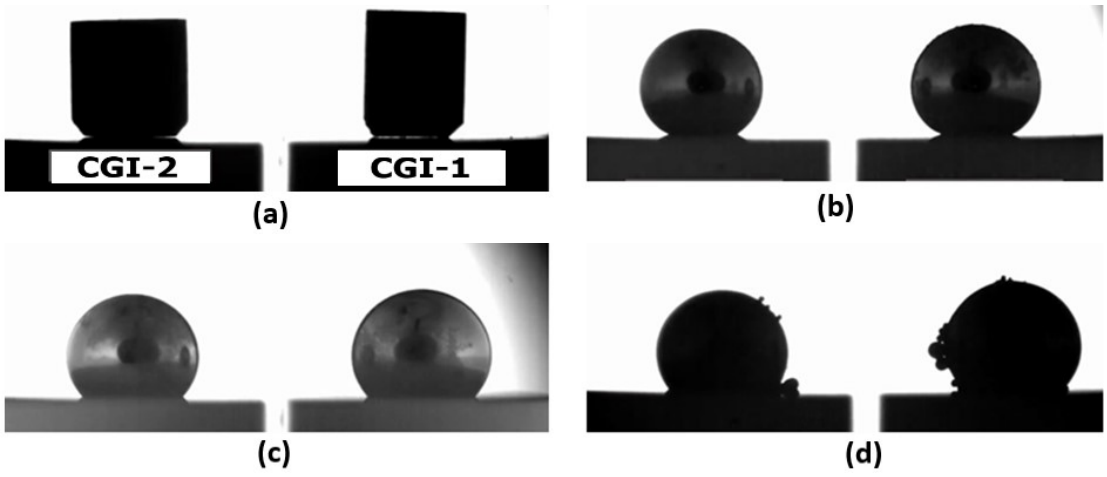

Fig. 2. Representative images taken from the movie of 2in1 sessile drop test of two CGI/Al_2O_3 couples: (a) the beginning of heating, T = 22°C; (b) the formation of the drop, T ~ 1199°C; (c) the end of the test at T = 1450°C for t = 15 min; (d) the last image recorded during cooling and corresponding to the end of wettability kinetic curves at T = 1141°C shown in Figs. 3a,b

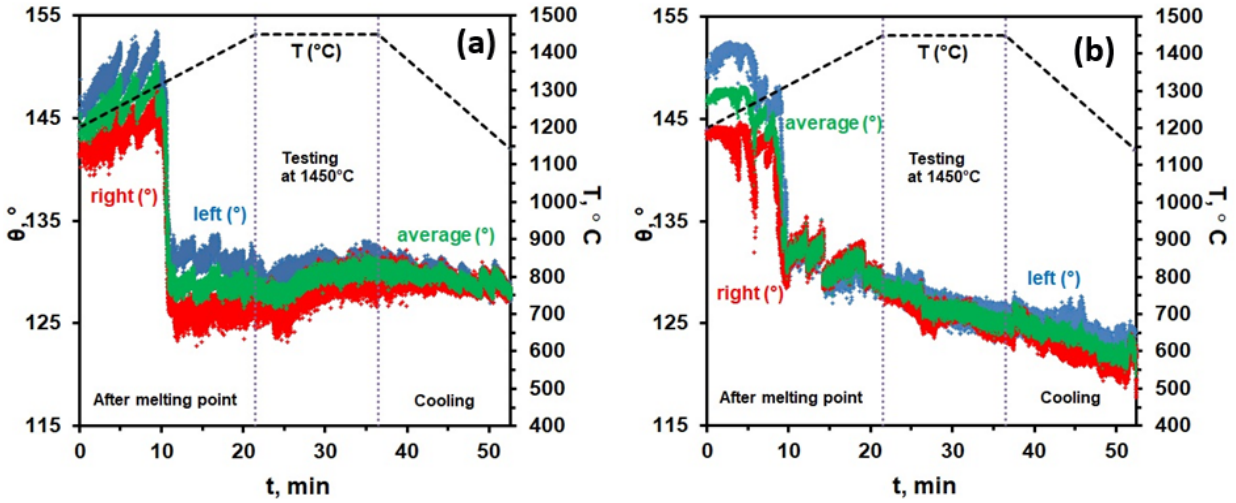

Fig. 3. Wettability kinetics of examined alloys of alumina substrates: (a) CGI-1; (b) CGI-2

TABLE 2

Summary of the sessile drop tests of CGI samples on Al_3O_3 substrates

CGI	θ^*			θ^0			θ^{15}			θ^f		
	θ_l^*	θ_r^*	θ_{av}^*	θ_l^0	θ_l^0	θ_{av}^0	θ_l^{15}	θ_l^{15}	θ_{av}^{15}	θ_l^f	θ_l^f	θ_{av}^f
CGI-0 [24]	149	147	148	133	129	131	132	130	131	131	131	131
CGI-1	147	143	145	131	127	129	132	128	130	129	127	128
CGI-2	150	144	147	128	128	128	126	124	125	122	120	121
θ^* – at 1199°C; θ^0 – at 1450°C for $t = 0$; θ^{15} – at 1450°C for $t = 15$ min; θ^f – final value measured at 1141°C												

drop surface during solidification. For both couples, the drops were detached from the substrate that made possible the detailed structural characterization of the revealed drop-side and the substrate-side interfaces. However, a few small daughter droplets were still well bonded either to the mother drop (e.g. Fig. 5b) or the substrate (e.g. Fig. 5c, Fig. 5d) that allowed their investigation and the drop/substrate interface characterization. The same above observations have been reported recently for the sessile drop couples of CGI alloys on Al_2O_3-rich substrates [38,39].

The microscopic characterization of cross-sectioned couples revealed important structural changes in both drops, as compared to their as-cast alloys. Particularly in the surface layer of the drops, vermicular graphite did not re-grow after remelting and afterward solidification of the alloys. On example of CGI-1/Al_2O_3 couple (Figs. 6a-d), it can be seen that graphite precipitates show non-uniform distribution and many graphite precipitates have changed their morphology from worm-like shape (typical for CGI) to flake one (typical for LGI) while spherical graphite precipitates were not noted to occur. This effect is the most pronounced in the surface layer of the solidified drop (Fig. 6b, Fig. 6c), especially in the vicinity of the triple line (Fig. 6c), as compared to the central part of the drop (Fig. 6d).

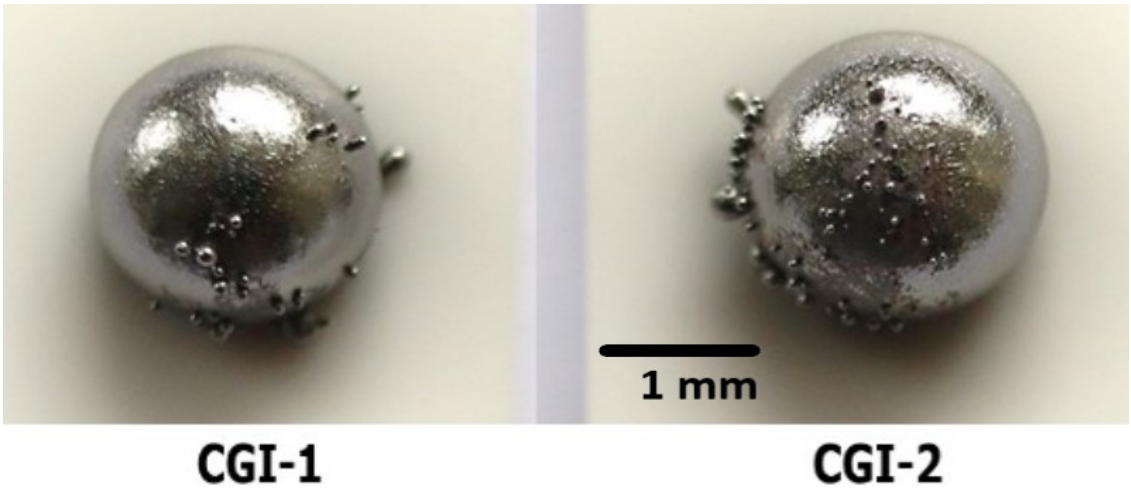

Fig. 4. Top-view photos of the solidified drops on alumina substrates after sessile drop tests

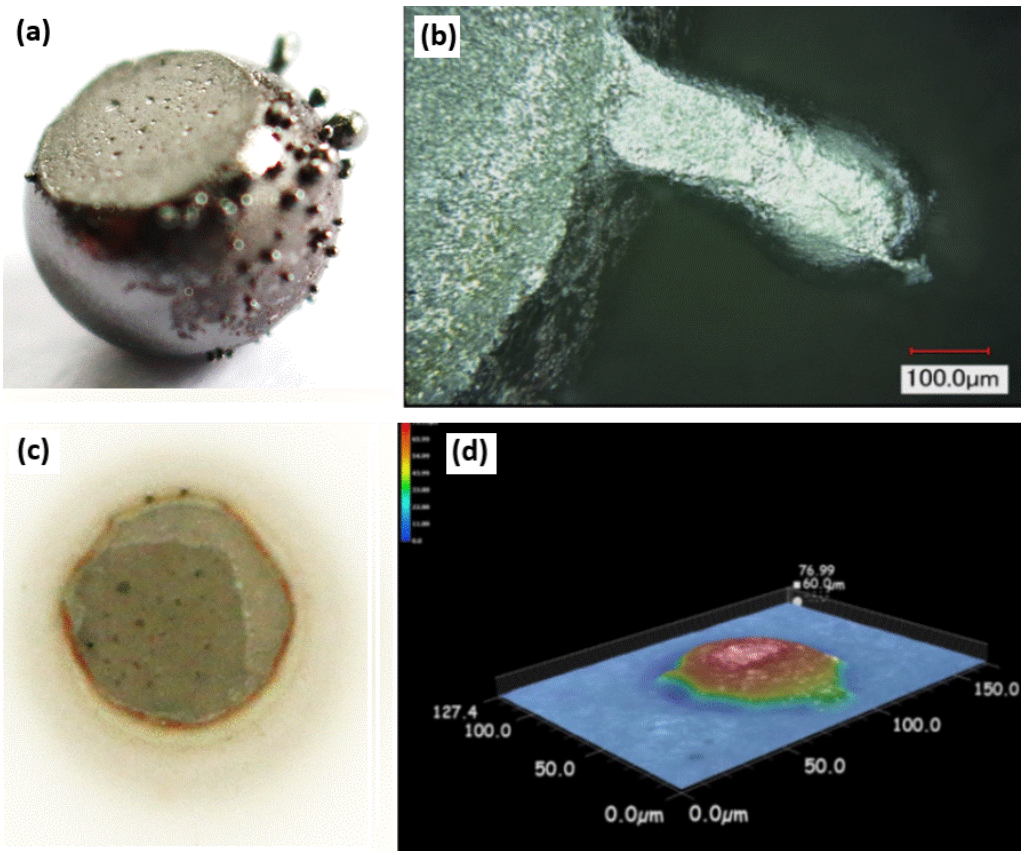

Fig. 5. Examination of CGI-1/Al_2O_3 couple after the sessile drop test: (a,b) bottom views of solidified drop detached from the substrate showing the formation of daughter droplets on the surface of mother drop; (c,d) top views of alumina substrate showing the contact area of the drop with the substrate and the formation of interfacial layer (a,c – photos; c,d – 3D-LM)

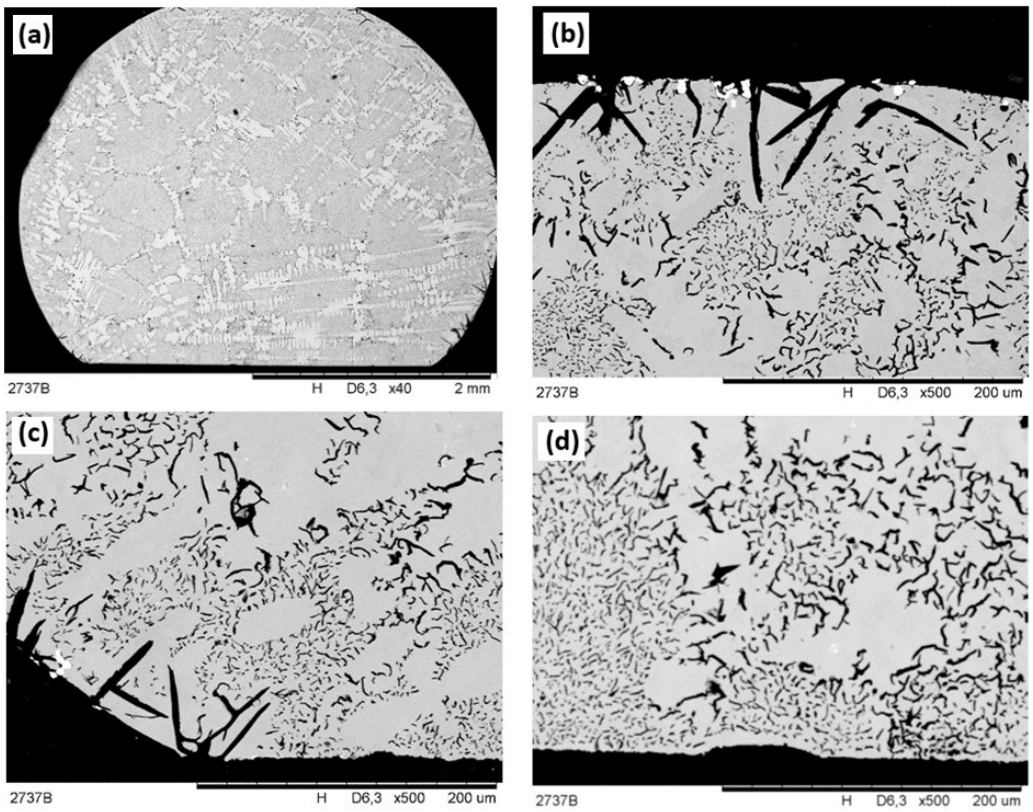

Fig. 6. SEM micrographs of cross-sectioned sessile drop couple CGI-1/Al_2O_3: (a) general view of whole drop; (b) top of the drop; (c) left-side of the drop bottom; (d) central part of the drop bottom

SEM observations of the CGI-1 drop showed also that the nucleation of flake graphite precipitates is accompanied with non-metallic inclusions both on the top of the drop (Fig. 6b) and on the drop surface near the vicinity of the triple line, e.g. close to the drop bottom (Fig. 6c). EDS analysis of these precipitates (Fig. 7 and Fig. 8, respectively) evidenced Mo, V, Mn and S thus suggesting the formation of complex sulfide $(Mo,V,Mn)S_2$. Important information was delivered from SEM observation of the CGI-1/Al_2O_3 couple under high magnification. As it is shown in Fig. 9a and Fig. 9b, the far is the distance from the drop surface the more graphite precipitates of worm-like morphology are in the drop. Furthermore, the presence of graphite layer is well distinguished at the drop-side interface being in contact with alumina substrates. Since during sessile drop test, the CGI-1 drop was *in situ* detached from alumina substrate, it was decided to examine the daughter droplet that was disconnected from the mother drop but still it remained well attached to the substrate (Fig. 10a). Its cross-section SEM observations (Figs. 10b,c), accompanied with EDS analysis, revealed similar findings as those for the mother drop, i.e. the degradation of vermicular graphite and nucleation of graphite on open surface of the droplet as well as at the alumina substrate. Moreover, EDS revealed the presence of Al in droplets due to the dissolution of the substrate in the molten alloy. Phenomena discussed above were also observed in our recent studies of CGI-0/Al_2O_3 [38] and LGI/Al_2O_3-ZrO_2-SiO_2 [39].

The detailed SEM investigation of the cross-sectioned substrate, *in situ* detached from the solidified mother CGI-1 drop (left part of Fig. 10b), provided very important information that helps to understand one of the crucial reasons of the reconstruction of the primary vermicular morphology of graphite to flake-like precipitates. From the analysis of the EDS maps of distribution of elements (Fig. 11), we may conclude that during high temperature interaction, Mg from molten alloy reacts with alumina substrate to form Mg-rich oxide layer at the substrate-side interface and this complex oxide plays a role of a seed for graphite nucleation. This reaction and evaporation of Mg contribute to the decrease of Mg content in the alloy, especially in the vicinity of the drop surface and its interface with the substrate, thus creating favorite conditions for the formation of flake graphite. These findings give experimental proofs of the essential role of metal sulfides and oxides as seeds for the nucleation of graphite in molten cast iron as well as the effect of Mg on the formation of compacted graphite precipitates. They are also consistent scientific concepts of graphite nucleation in iron-based alloys discussed in [20-29].

Figures 12-14 show the most representative results of structural characterization of the CGI-2/Al_2O_3 couple those analysis releases the same findings as for the CGI-1/Al_2O_3 sessile drop test, i.e.: 1) *in situ* detachment of the drop from the substrate during cooling (Fig. 12a); 2) the formation of daughter

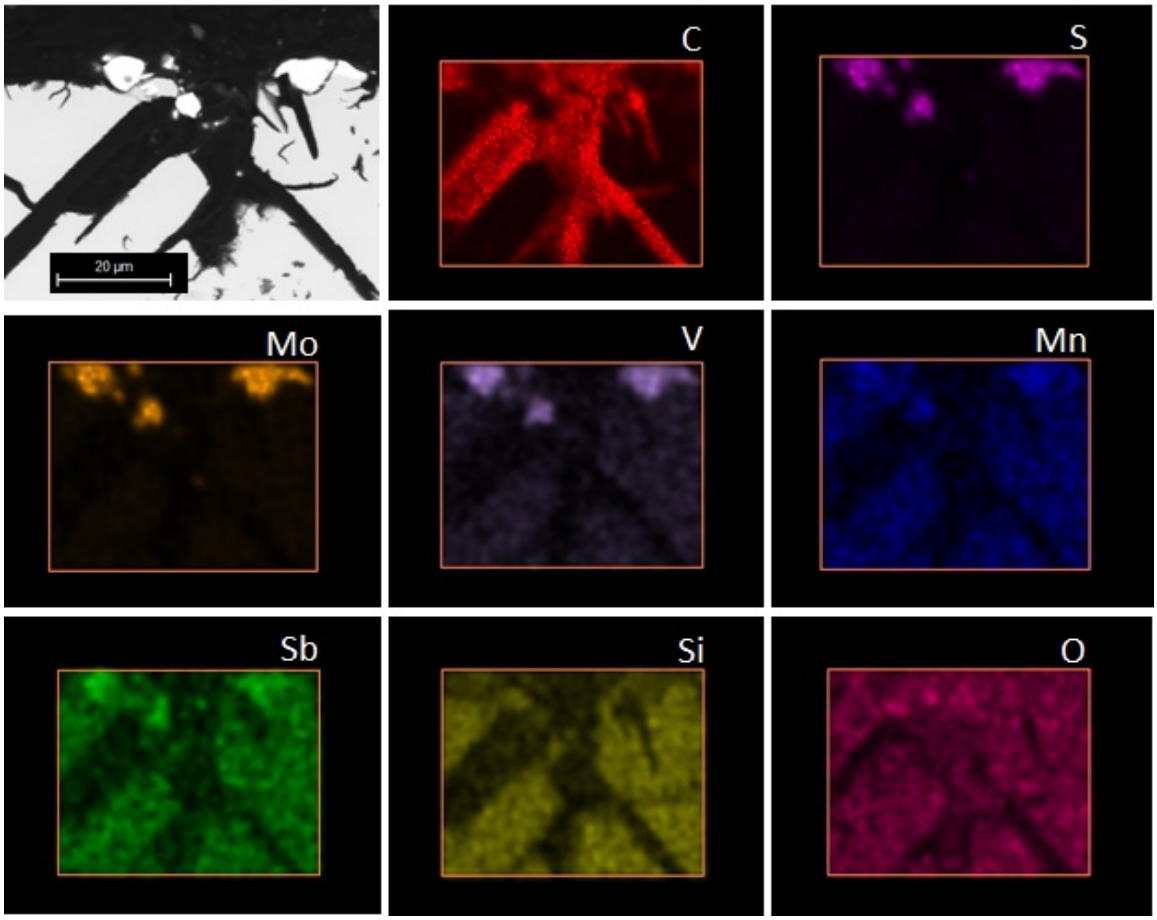

Fig. 7. SEM micrograph of cross-sectioned CGI-1/Al_2O_3 couple and corresponding local EDS maps of distribution of selected elements taken from the top of the drop

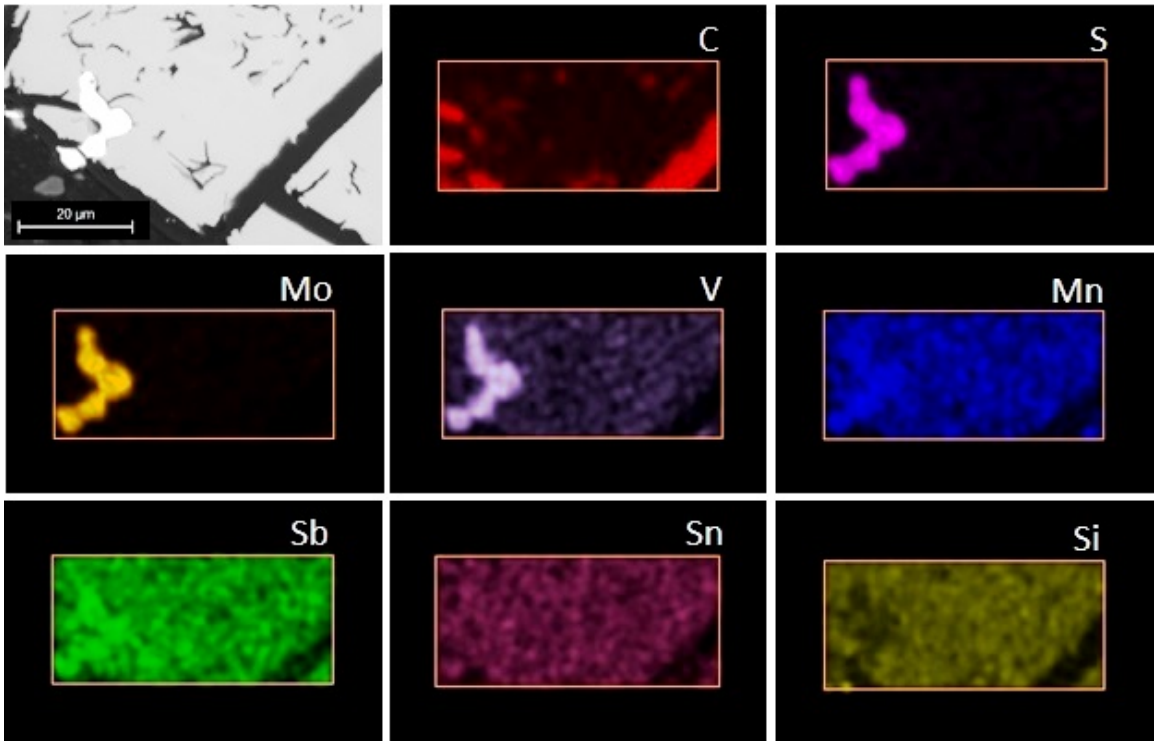

Fig. 8. SEM micrograph of cross-sectioned CGI-1/Al_2O_3 couple and corresponding local EDS maps of distribution of selected elements taken from the drop bottom

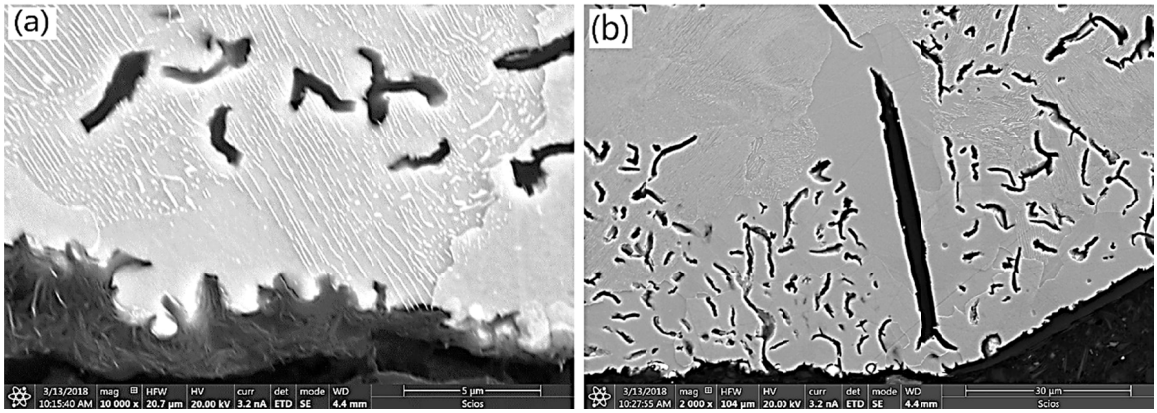

Fig. 9. High resolution SEM images of interface structure formed between CGI-1 drop and alumina substrate during sessile drop test: (a) central part of the drop; (b) right side of the drop in the vicinity of triple line

droplets on the surface of the mother drop during solidification (Figs. 12b-d and Fig. 13d); 3) the reactively changed surfaces of both the drop-side (Fig. 12a) and substrate-side of the interface (Figs. 12c,d); 4) after remelting, holding at high temperature of the sessile drop test and subsequent cooling, the decrease of the vermicular graphite precipitates and almost disappearance of spherical graphite (Figs. 13a-c) accompanied with the nucleation of flake-like graphite, mainly at the surface of the mother drop (Fig. 13) and the daughter droplets (Fig. 13b); 5) the presence of reactively formed Mg-rich interfacial layer of complex oxide at the substrate-side interface (Fig. 14); 6) nucleation of graphite either on the surface of metal sulfite (Mo,V,Mn)S_2 and/or of oxides (Al_2O_3 or Mg-rich complex oxide). Moreover, in case of CGI-2 alloy containing two times greater amount of Mg, the surface of cross-sectioned substrate contacted with CGI-2 drop had increased concentration of S and P (Fig. 14). We suggest that it might be related with the formation of MgS_2 or metal phosphides that may also ease heterogeneous nucleation of graphite.

It should be highlighted that compared to the CGI-1 alloy, CGI-2 showed better wetting of alumina substrate (measured by the value of contact angle, Fig. 2a and Fig. 2b, respectively). We suggest that much higher Mg content is responsible for wettability improvement due to a greater reactivity of the alloy. It was well evidenced by more pronounced change of both the drop bottom structure (Fig. 12a) and substrate surface structure (Fig. 12c, Fig. 12d) as well as by almost twice thicker interfacial reaction product of Mg-rich complex oxide (Fig. 14), i.e. 6-8 µm vs 2-4 µm.

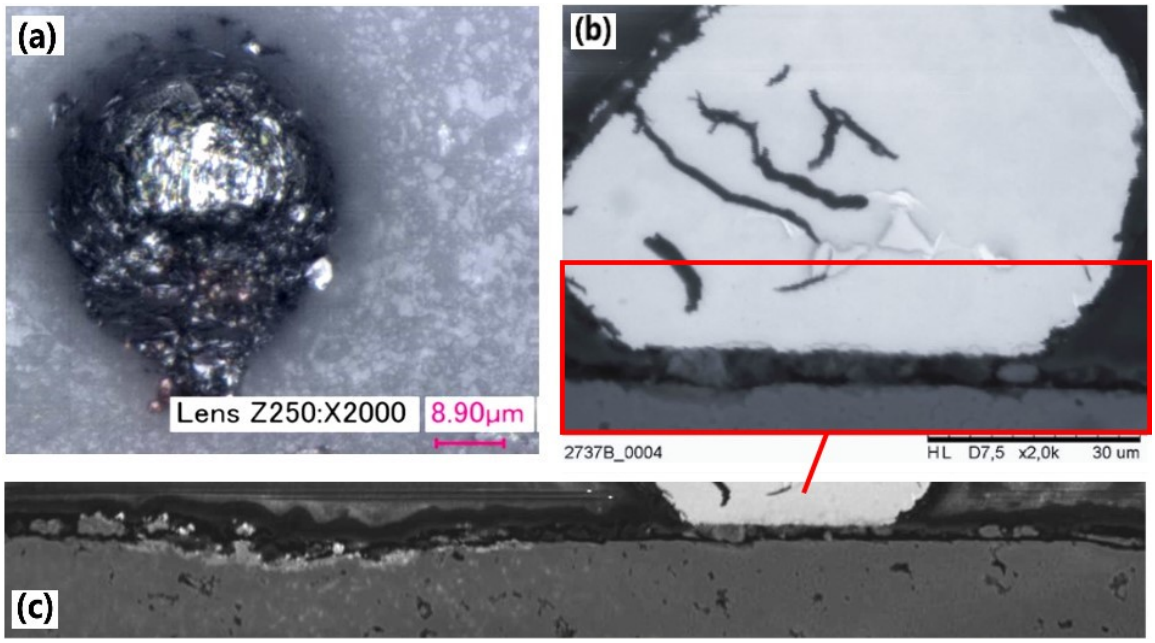

Fig. 10. Daughter droplet formed at the surface of solidifying mother drop of CGI-1 alloy and well bonded to the substrate: (a) top 3D-LM view; (b,c) SEM cross-section views of the droplet/substrate interface; a red box in (b) shows the magnified part of (c)

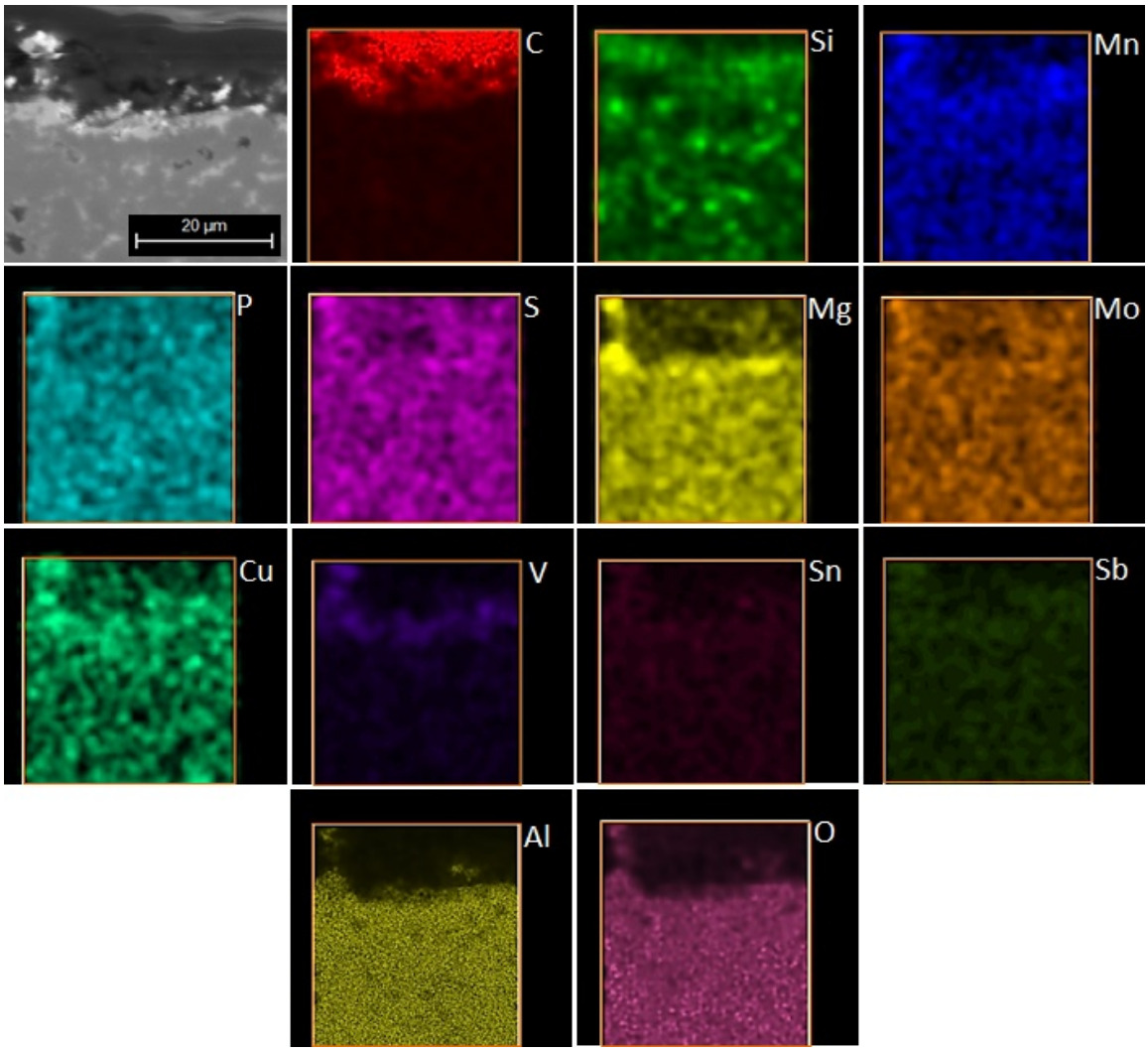

Fig. 11. SEM micrograph of cross-sectioned Al_2O_3 substrate after high temperature interaction with CGI-1 drop and corresponding local EDS maps of distribution of selected elements

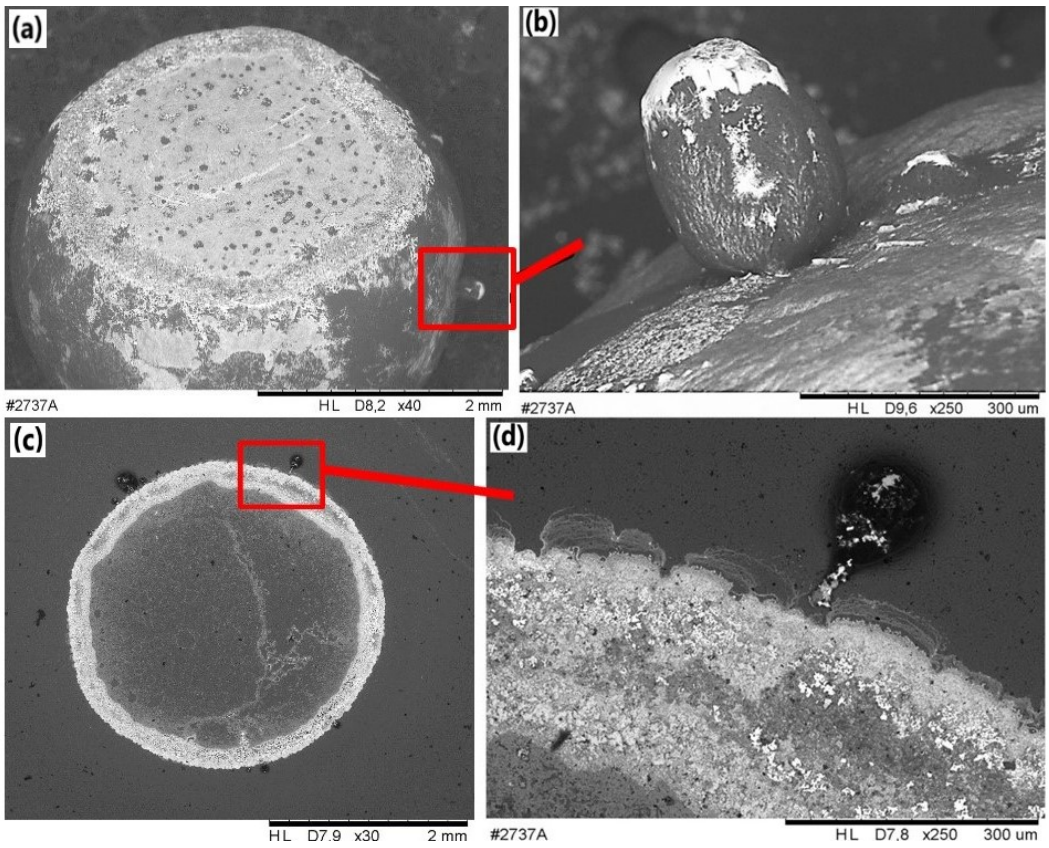

Fig. 12. Top-view SEM micrographs of CGI-2/Al_2O_3 couple: (a) the drop bottom; (b) the open surface of the drop; (c,d) substrate surface that was in contact with the drop

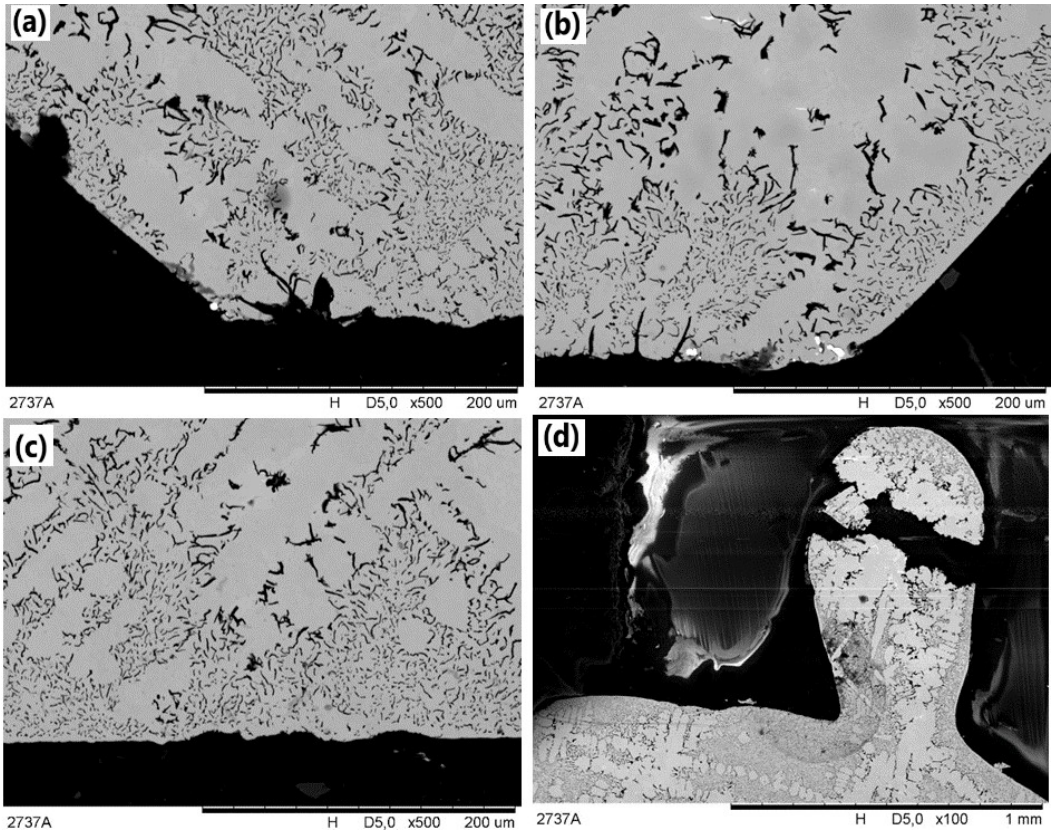

Fig. 13. SEM micrographs of cross-sectioned sessile drop couple CGI-2/Al_2O_3: (a,b) drop bottom (a – left side; b – right-side of the drop); (c) central part of the drop bottom; (d) daughter droplet squeezed from the mother drop during solidification that was broken during cutting the couple for structural observation

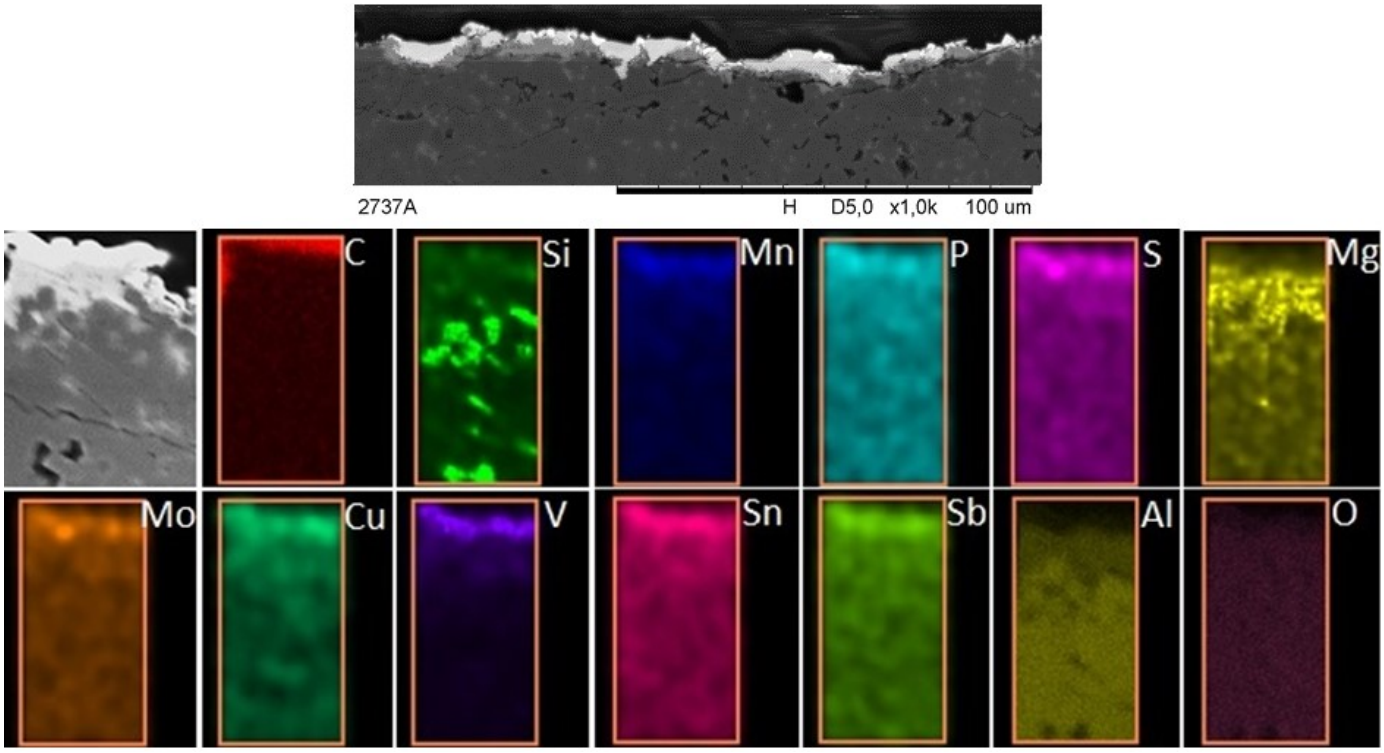

Fig. 14. SEM micrograph of cross-sectioned Al_2O_3 substrate after high temperature interaction with CGI-2 drop (substrate-side interface) and corresponding local EDS maps of distribution of selected elements

4. Conclusions

1. For the first time, the sessile drop method was applied for real-time observation of the effect of alloying compacted graphite cast iron on its melting, wetting and solidification behavior when placed on alumina substrate. Comparative study has been performed with three CDIs, i.e. unalloyed CGI and those containing the same amounts of Mo, V, Sn and Sb and dissimilar amounts of Mg + Cu.
2. All selected alloys show non-wetting behavior of alumina with the contact angle values slightly decreasing with increase in Mg + Cu concentration. It suggests that for synthesis CGI-alumina composites by liquid- assisted techniques, further improvement of physico-chemical compatibility between the metal matrix and the oxide reinforcement is needed, e.g. by covering the reinforcement with wettable coatings.
3. During cooling after sessile drop tests, the solidification of all alloys was accompanied with the formation of small satellite droplets on the surface of the mother drops due to volume expansion of eutectic constituent of the melt. This phenomenon may play beneficial role in the production of porosity-free cast iron components.
4. Structural characterization of solidified couples showed the reactively formed Mg-rich oxide layer at the substrate surface of which thickness increases with increase of Mg content in the alloy. Besides Mg evaporation, the formation of this layer resulted in the partial consumption of Mg from the remelted alloys and segregation of Mg concentration in the drops. As consequence, after remelting and heating on alumina substrates, the solidification of cast iron drops was accompanied with the formation of graphite precipitates of flake-like morphology instead of compacted graphite. This phenomenon was particularly noticeable in the near surface regions that after sessile drop test, became depleted in Mg. These findings should be taken into account when metal casting or testing of molten CGI alloys is accompanied with high surface to volume ratio, e.g. (1) casting of thin wall components or (2) testing of CGI thermophysical properties by small container-assisted methods, such as calorimetry and thermal analysis, because they may affect the reliability of measurements.

Acknowledgements

This research was financed by the National Science Centre of Poland in frame of OPUS program (project No. 2015/17/B/ST8/03391). Technical assistance of Dr. A. Polkowska (high resolution SEM characterization on FEI SciosTM microscope) is acknowledged.

SUPPLEMENTARY MATERIAL

Movie 1: The online version of this article contains supplementary material, which is available to authorized users. It presents the movie of the sessile drop test performed with two CGI/alumina couples simultaneously using 2in1 procedure (left – CGI-2; right – CGI-1).

REFERENCES

[1] D.M. Stefanescu, A histrory of cast iron, in: ASM Handbook, ASM Handbook, vol. 1A Cast Iron Science and Technology, ASM International (2017).

[2] E. Nechtelberger, H. Puhr, J.B. Nesselrode, A. Nakayasu, Cast iron with vermicular/compacted graphite – state of the art. Development, production, applications, in: Proc. 49th International Foundry Congress, Chicago, USA, CIATF (1982).

[3] H. Qiu, Z. Chen, China Foundry **4**, 261-269 (2007).

[4] M. Holtzer, M. Górny, T. Dańko, Microstructure and Properties of Ductile Iron and Compacted Graphite Iron Castings. The Effects of Mold Sand/Metal Interface Phenomena. SpringerBriefs in Materials (2015).

[5] M.A. Suhaimi, K.H. Park, S. Sharif, D.W. Kim, A.S. Mohruni, Evaluation of cutting force and surface roughness in high-speed milling of compacted graphite iron, in: MATEC Web of Conferences, EDP Sciences, 101, 03016, SINCEST (2016).

[6] S. Dawson, Compacted graphite cast iron – a material solution for modern diesel engine cylinder blocks and heads, in: Proc. 68th Word Foundry Congress, Chennai, India, The Institute of Indian Foundrymen (2008).

[7] J.D. Altstetter, R.M. Nowicki, Trans. AFS **82-188**, 959-970 (1982).

[8] Y. Tanaka, H. Saito, K. Ikawa, J. Japan Foundrymen's Soc. **53** (4), 187-192 (1981).

[9] R.W. Gregorutti, J.E. Gru, Int. J. Cast. Metal. Res. **27** (5), 275-281 (2014).

[10] E. Guzik, S. Dzik, Archives Foundry Eng. **9** (1), 175-180 (2009).

[11] P.V. Palmer, Foundry Trade Metals **32223**, 574-580 (1981).

[12] P. Ponicky, P. Socovsky, Liatiny s cervikovitym grafitom begowane cinom a medou, Slevarenstvi **6** (1988).

[13] A. Pytel, K. Sękowski, Perlitic vermicular graphite cast iron, in: M.S.J. Hashimi and L. Looney (Eds.) Proc. Int. Conf. Advances in Materials and Processing Technologies, AMPT'99 and 16th Ann. Conf. of the Irish Manufacturing Committee, IMC16, **vol. III**, Dublin City University (1998).

[14] I. Riposan, M. Chisamera, Legierte Gusseisen mit Vermikulargraphit. Giesserei-Praxis **11**, 161-173 (1985).

[15] E. Guzik, Archiwum Odlewnictwa **6** (21/1), 33-42 (2006).

[16] G.I. Sil'man, V.A. Teikh, G. S. Sosnovskaya, Litein. Proizv. **10**, 8-9 (1975).

[17] G.I. Sil'man, V.V. Kamynin, A.A. Tarasov, Met. Sci. Heat Treat. **45**, 7-8 (2003).

[18] A. De Sy, Giesserei **2**, 25-32 (1964).

[19] B. Bihari, R. Kumar, A.K. Singh, Int. J. Eng. Res. Techn. **3** (5), 81-84 (2014).

[20] A.I. Fedyanin, Effect of heat treatment on the structural, mechanical, and antifriction properties of AChS-5 cast iron, in: Metal Science and Heat Treatment, KPI, Kalinin (1976).

[21] D.M. Stefanescu, L. Dinescu, S. Craciun, M. Popescu, Production of vermicular graphite cast iron by operative control and correction of graphite shape, in: Proc. 46th Int. Foundry Congress, CIATF Madrid, Spain (1979).

[22] H. Itofuji, Y. Kawano, N. Inoyama, S. Yamamoto, B. Chang, T. Nishi, The formation mechanism of compacted/vermicular graphite in cast irons, AFS Transactions **91**, 831-840 (1983).

[23] I. Riposan, M. Chisamera, C. Stan, C. Hartung, D. White, Mater. Sci. Techn. **26** (12), 1439-1447 (2010).

[24] D.M. Stefanescu, G. Alonso, P. Larrañaga, E. De la Fuente, R. Suarez, Acta Mater. **107**, 102-126 (2016).

[25] D.M. Stefanescu, G. Alonso, P. Larrañaga, E. De la Fuente, R. Suarez, Acta Mater. **139**, 109-121 (2017).

[26] D.M. Stefanescu, G. Alonso, P. Larrañaga, E. De la Fuente, R. Suarez, Int. J. Metalcast. **12**, 722-752 (2018).

[27] de A. Vicente, J.R. Sartori Moreno, T.F. de A. Santos, D.C.R., Espinosa, J.A.S. Tenório, J. Alloy Comp. **775**, 1230-1234 (2019).

[28] G. Alonso, D.M. Stefanescu, P. Larrañaga, R. Suarez, Int. J. Metalcast. (2020) https://doi.org/10.1007/s40962-020-00441-2

[29] G. Alonso, D.M. Stefanescu, R. Suárez, A. Loizaga, G. Zarrabeitia, Int. Foundry Res. **66** (4), 2-12 (2014).

[30] Tadesse, H. Fredriksson, Int. J. Cast Metals Res. **30** (3), 159-170 (2017).

[31] R.M. Hathaway, P. Rohatgi, N. Sobczak, J. Sobczak, Ferrous composites: a review, in: N. Eustathopoulos, N. Sobczak (Eds.), Proc. 2nd Int. Conf. High Temperature Capillarity, 1997, Cracow, Poland, Foundry Research Institute (1998).

[32] M. Bay, Y. Su, S-W. Gong, Preparation and properties of high chromium cast iron matrix composites reinforced by zirconium corundum particles, in: Proc. 2nd Int. Conf. Test, Measurement and Computational Method (TMCM-2017), 365-369 (2017).

[33] N. Dulska A. Studnicki, J. Szajnar, Reinforcing cast iron with composite insert, Arch. Metall. Met. **62** (1), 355-357 (2017).

[34] N. Sobczak, M. Singh, R. Asthana, Curr. Opin. Solid St. Mater. Sci. **9**, 241-253 (2005).

[35] Y.A. KIyachko, L.L. Kunin, Zhurnal Prikladnoy Khimii **22** (7), 707-715 (1947) (in Russian).

[36] S.I. Popel, Wetting of refractory materials with molten metal and slag, in: Foundry Theory and Practice Masbgiz, Sverdlovsk, (1959) (in Russian).

[37] N.V. Pitak, R.M. Fedoruk, R.S. Shulyak, T.P. Khmelenko, Refractories **19** (5-6), 301-304 (1978).

[38] M. Bacior, N. Sobczak, M. Homa, P. Turalska, A. Kudyba, G. Bruzda, R. Nowak, A. Pytel, Trans. Found. Res. Inst. **4**, 375-384 (2017).

[39] N. Sobczak, J.J. Sobczak, M. Kolev, L. Drenchev, P. Turalska, M. Homa, A. Kudyba, G. Bruzda, J. Mater. Eng. Perf. **29**, 2499-2505 (2020).

[40] M. Homa, N. Sobczak, P. Turalska, G. Bruzda, M. Bacior, M. Warmuzek, A. Polkowska, Trans. Found. Res. Inst. **LVII** (4), 345-350 (2017).

[41] N. Sobczak, R. Nowak, W. Radziwiłł, J. Budzioch, A. Glenz, Mater. Sci. Eng. **495** (1-2), 43-49 (2008).

[42] N. Sobczak, J. Sobczak, R. Asthana, R. Purgert, China Foundry **7** (4), 425-437 (2010).

[43] ASTRA Reference Book, IENI, Report, Oct. 2007.

[44] L. Liggieri, A. Passerone, High Temp. Techn. **7** (2), 80-86 (1989).

[45] H. Fujii, S. Izutani, T. Matsumoto, S. Kiguchi, K. Nogi, Mater. Sci. Eng. A **417** (1-2), 99-103 (2006).

[46] K. Kondoh, M. Kawakami, H. Imai, J. Umeda, H. Fujii, H. Acta Mater. **58** (2), 606-614 (2010).